SCIENCE CHINA PRESS

SCIENCE CHINA Chemistry 2026 69(5): 2463–2470
https://doi.org/10.1007/s11426-025-3011-9

ARTICLES

De novo design of A-D-A-structured acceptors with a high photoluminescence quantum yield and crystallinity for 20.2%-efficiency organic solar cells

Peiran Wang[1,2], Jia Wang[1], Yanyi Zhong[3], Jiangbin Zhang[3], Tainan Duan[4,5], Jiaying Wang[1], Zhe Zhang[2], Zheng Xu[2], Jian Liu[2], Xiangjian Wan[2], Bin Kan[1*] & Yongsheng Chen[2*]

[1]School of Materials Science and Engineering, National Institute for Advanced Materials, Nankai University, Tianjin 300350, China
[2]State Key Laboratory and Institute of Elemento-Organic Chemistry, Frontiers Science Center for New Organic Matter, The Center of Nanoscale Science and Technology and Key Laboratory of Functional Polymer Materials, Renewable Energy Conversion and Storage Center (RECAST), College of Chemistry, Nankai University, Tianjin 300071, China
[3]College of Advanced Interdisciplinary Studies, National University of Defense Technology, Changsha 410073, China
[4]Chongqing Institute of Green and Intelligent Technology, Chinese Academy of Sciences, Chongqing 400714, China
[5]Chongqing School, University of Chinese Academy of Sciences, Chongqing 400714, China
*Corresponding authors (email: kanbin04@nankai.edu.cn; yschen99@nankai.edu.cn)

Received 23 July 2025; Accepted 11 September 2025; Published online 4 January 2026

Abstract Designing acceptors with high photoluminescence quantum yield (PLQY) and high crystallinity is crucial for minimizing non-radiative energy losses (ΔE_3) and realizing highly efficient organic solar cells (OSCs). Herein, we report three acceptor-donor-acceptor acceptors (GM series) featuring a novel centrally extended structure. Following the structural characteristics of GM2 and GM3, GM4 exhibits a distorted conformation of its central unit that reduces molecular packing density, leading to an enhanced PLQY. Despite its nonplanar geometry, the central unit maintains participation in efficient "C/C" molecular packings. Besides, benefiting from the brominated fused-ring structure, GM4 exhibits decreased energy disorder and enhanced crystallinity. As a result, binary OSCs leveraging GM4 demonstrate a high open-circuit voltage (V_{OC}) and an exceptionally low ΔE_3, resulting in a power conversion efficiency (PCE) of 16.5%. When incorporated as a guest acceptor into the D18:L8-BO films, GM4 optimizes the ternary film morphology, enhancing exciton generation and charge transport. Consequently, the D18:L8-BO:GM4 ternary device reached a maximum PCE of 20.2%, with simultaneous improvements in V_{OC}, short-circuit current density, and fill factor. This study not only expands a new molecular design strategy, but also demonstrates that appropriate regulation of molecular packing density is an effective strategy for achieving a high PLQY and crystallinity.

Keywords organic solar cells, A-D-A type acceptor, PLQY, crystallinity, non-radiative energy loss

1 Introduction

Organic solar cells (OSCs) have emerged as a promising renewable energy technology due to their distinctive advantages, such as cost-effectiveness, tunable optical properties, mechanical flexibility, and lightweight characteristics [1–4]. Over the past decade, significantly efforts have been devoted to advancing the OSC performance through molecular design [5–10], morphology optimization [11–13], interface engineering [14–16], and device architecture innovation [17–19], with the primary goal of achieving higher power conversion efficiencies (PCEs). Notably, molecular design plays a pivotal role as it governs both the photophysical properties and the packing behavior, thereby affecting the morphology of the active layer. Driven by continuous advancements in small-molecule acceptors (SMAs) with the framework of acceptor-donor-acceptor (A-D-A), state-of-the-art single-junction OSCs have achieved impressive PCEs exceeding 20%. However, further improving the PCE of single-junction OSCs remains challenging. A key limitation is that the open-circuit voltage (V_{OC}) of OSCs is still below 80% of the Shockley-Queisser (SQ) limit, primarily due to the large nonradiative energy loss (ΔE_3) in realistic OSCs [20].

It has been demonstrated that ΔE_3 in OSCs can be effectively reduced by enhancing the photoluminescence quantum yield (PLQY) of active-layer materials-the decisive factor for improving their external quantum efficiency of electroluminescence (EQE_{EL}) [21,22]. This fundamental understanding underscores the importance of developing novel photovoltaic materials with high PLQY for suppressing ΔE_3 and the total energy loss (E_{loss}) in OSCs [23]. Furthermore, simultaneous optimization of both short-circuit current density (J_{SC}) and fill factor (FF) is essential for attaining superior device performance with high PCEs. This performance metric is governed by efficient charge carrier transport and suppressed charge recombination in the active layer, both of which are mostly determined by the tight and well-ordered molecular packing of photoactive materials [24]. However, as per the aggregation-caused quenching (ACQ) mechanism, the close packing of planar organic molecules enhances π-π stacking, which promotes excimer formation in the excited state. This electronic interaction enhances intermolecular coupling, thereby accelerating nonradiative decay pathways while concurrently quenching fluorescent emission [25].

Therefore, it can be anticipated that appropriately reducing molecular packing could enhance the PLQY, leading to a lower ΔE_3. This principle is exemplified by an A-D-A structured acceptor DM-F [26], where strategic incorporation of a rigid three-dimensional norbornyl group into the central core of Y-molecular effectively

Citation: Wang P, Wang J, Zhong Y, Zhang J, Duan T, Wang J, Zhang Z, Xu Z, Liu J, Wan X, Kan B, Chen Y. *De novo* design of A-D-A-structured acceptors with a high photoluminescence quantum yield and crystallinity for 20.2%-efficiency organic solar cells. *Sci China Chem*, 2026, 69: 2463–2470. https://doi.org/10.1007/s11426-025-3011-9

suppresses the excessive aggregation of acceptors. Consequently, the high PLQY characteristic of DM-F enables a high EQE_{EL} and an extremely low ΔE_3 of 0.14 eV. In our previous work, we developed CH-series acceptors through strategic conjugation extension of central units [27,28]. These materials systematically demonstrated the central unit's governing influence on molecular packing behavior and its direct correlation with device performance. Specifically, the central extension unit promotes both "C/C" and "C/E" molecular packing motifs, which are fundamentally responsible for establishing the optimal three-dimensional (3D) intermolecular packing network in Y-series acceptors. Such a unique 3D network is recognized as the key determinant enabling their effective charge dynamics and highly-efficient performance [29,30]. These collective insights establish a dual-optimization principle for high-efficiency SMAs: synergistic enhancement of PLQY through controlled aggregation while maintaining superior charge transport via precisely engineered 3D molecular stacking [31].

Based on these considerations, we developed a novel SMA, designated as GM4, through a rational molecular engineering strategy. First, we used thiophene units to extend the molecular backbone via single bonds, obtaining GM2. The rotational freedom of these single bonds conferred a nonplanar conformation, which effectively suppressed dense molecular packing and consequently enhanced the PLQY. However, this freely rotating conformation also increased energy disorder and reorganization energy, leading to a high radiative energy loss. To address these limitations, we synthesized GM3 by further constructing fused-ring aromatic backbones based on GM2, thereby locking the molecular conformation. This approach followed the strategy of conjugation extension while removing the electron-deficient aromatic ring, introducing steric hindrance between the central unit and the backbone. The steric hindrance disrupted molecular planarity to some extent, reducing molecular packing and thereby maintaining the high PLQY of GM2. Finally, we employed a bromination strategy to generate GM4, which balanced reduced packing density with enhanced crystallinity. As expected, GM4 exhibited a higher PLQY compared to acceptors with a planar central unit, leading to an exceptionally low ΔE_3 of 0.175 eV and a high V_{OC} of 0.975 V, reaching near 82% of the SQ limit. Despite its loosely packed structure, GM4 retained high crystallinity due to bromine-induced intermolecular interactions. As a result, the D18:GM4 binary device achieved a satisfactory PCE of 16.5%, showcasing its potential as an efficient acceptor. Furthermore, due to suppressed ΔE_3 and optimized morphology, the D18:L8-BO:GM4 ternary OSC achieved an outstanding efficiency of 20.2%-among the highest reported for OSCs. This work demonstrates that strategically balancing molecular planarity, packing density, and crystallinity can simultaneously minimize ΔE_3 and maximize device performance.

2 Results and discussion

2.1 Material synthesis and properties

In this study, the conceptual and synthetic landscape of centrally extended acceptors was further expanded. Figure 1a illustrates the chemical structures of GM2, GM3, and GM4, while Scheme S1 (Supporting Information online) provides their detailed synthetic routes. Firstly, compound **1** was synthesized following established methods reported in the literature. Unlike traditional condensation reactions between *ortho*-diimine and *ortho*-diamines, we utilized 2-thienylmagnesium bromide to modify the molecular backbone, creating a new approach for further modification based on the Y-backbone. This intermediate was then condensed via a dihydroxylation reaction to obtain compound **2**. Subsequently, compound **3** was synthesized efficiently using a Vilsmeier-Haack reaction, followed by a high-yielding Scholl reaction to construct compound **4**. After successfully establishing the fused-ring core structure, bromination of the central unit yielded compound 5. Finally, the target acceptor GM4 was ultimately obtained through a Knoevenagel condensation reaction between compound **5** and 2-(5,6-difluoro-3-oxo-2,3-dihydro-1H-inden-1-ylidene) malononitrile (IC-2F). Notably, this streamlined synthetic pathway simultaneously provided access to intermediate acceptors GM2 and GM3 in high yields (Scheme S1), demonstrating the efficiency and versatility of our synthetic design.

Density functional theory (DFT) calculations revealed the A-D-A structure of GM4, as characterized by the peak-valley-peak feature in the frontier orbital charge density difference (ΔQ) (Figure 1b and Figure S1, Supporting Information online). Meanwhile, due to the electron-rich characteristic of the thiophene unit, increased electrostatic surface potential of the central core of GM-series molecules can be observed (Figure 1c). This electronic structure transformation may partially show the largely unexplored diversity of Y-series molecules with central-unit modifications, offering an effective and convenient approach for constructing typical and high-performance A-D-A-type acceptor. To explore the effects of this new conjugation extension on molecular geometries and packing behavior, single-crystal X-ray diffraction measurements of GM4 were performed. Detailed X-ray parameters and structure factors, along with the structural outputs of the single crystal, are provided in Table S1 (Supporting Information online) (CCDC number: 2432920). As shown in Figure 1d, the hexyl and decyl substitutions on the SMAs are omitted for easy observation. Unlike CH-series molecules featuring extended conjugation through a phenazine-ring system, there are no non-covalent interactions between the central unit of GM4 and the S atom of the backbone. Owing to the distorted conformation of the central unit, the GM4 molecule does not exhibit a planar molecular backbone. In particular, there is a large dihedral angle of 34.5° between the backbone and central unit, which may reduce molecular packing to some extent.

To verify this speculation, the packing coefficients of the average distance were calculated. As presented in Table S2, GM4 has a lower packing coefficient of 53.2% compared to L8-BO (64.1%) [32], indicating a looser molecular arrangement in GM4. As shown in Figure 1d, the favorable three-dimensional (3D) molecular packing networks are well established, featuring a rectangular void of approximately 23.57 Å × 19.20 Å. The diverse 3D molecular packing of GM4 and L8-BO is likely attributed to differences in their intermolecular packing modes. In addition to two common packing modes ("E/E" mode and "dual E/b" mode) observed in both molecules, a third packing mode ("C/C" mode) was also identified in GM4 (Figure 1e), indicating that the distorted central unit with a large conjugation area also participates in the packing behavior. More importantly, the "C/C" mode enables a highly efficient charge transfer process, similar to the two other stacking modes, offering an opportunity to establish isotropic charge transport networks while maintaining appropriate intermolecular distances in the corresponding films.

To further shed light on the aggregation behavior of GM4 and L8-BO, the grazing-incidence wide-angle X-ray scattering (GIWAXS) measurements were employed for neat films. As shown in Figure S2 and Table S3, all neat films presented obvious (010) and (100) diffraction peaks in out-of-plane (OOP) and in-plane (IP) directions, indicating their favorable face-on orientation of the molecular packing. Note that GM4 yielded a larger π-π distance of 3.90 Å than that of L8-BO (3.80 Å) in OOP direction, suggesting a loose packing behavior for GM4, which agrees well with the single crystal data.

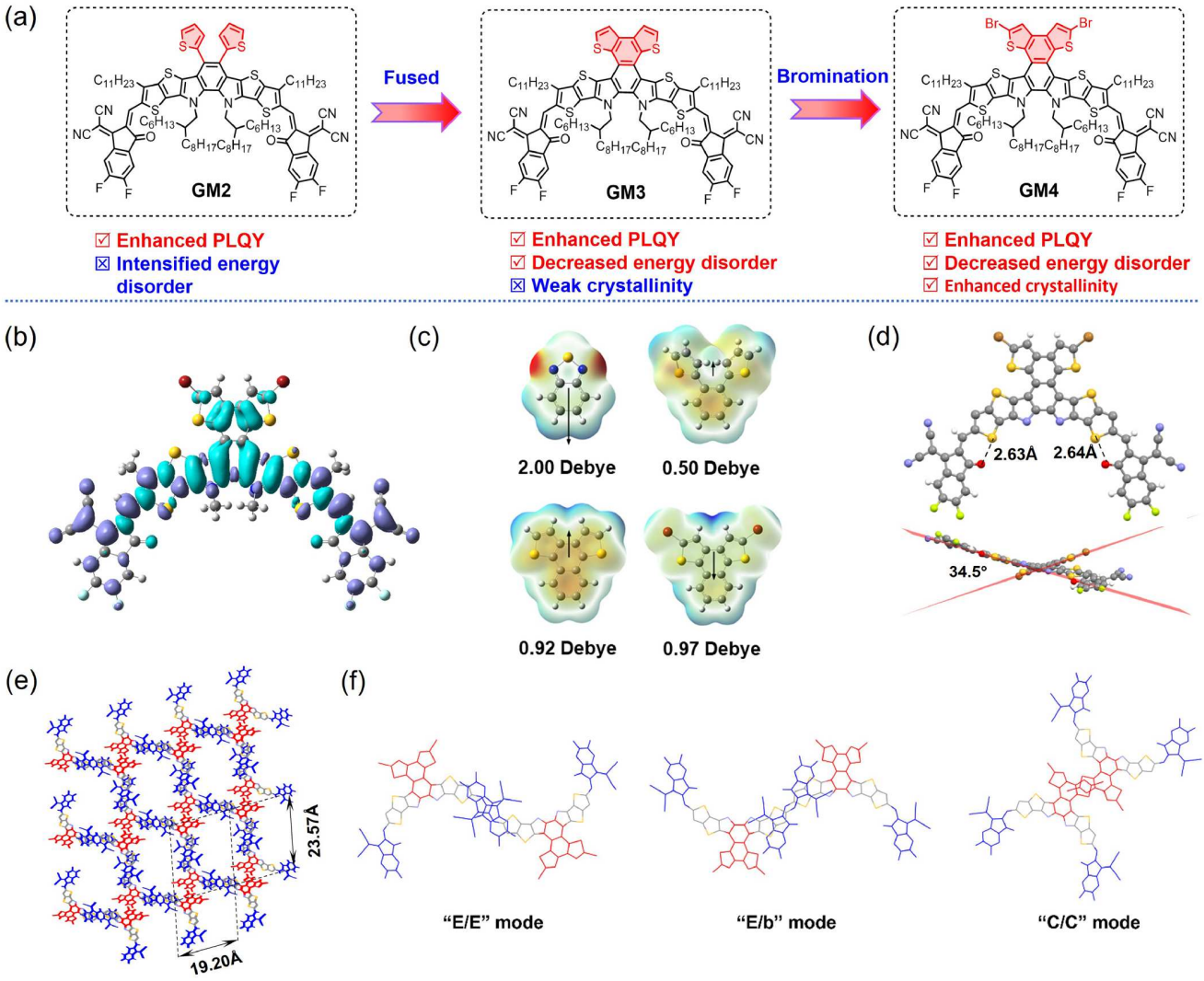

Figure 1 (Color online) (a) Molecular design of the GM-series acceptors. (b) Theoretical density distribution $\Delta Q = \Psi^2_{LUMO} - \Psi^2_{HOMO}$ along the longest axis (backbone) of GM4. (c) Electrostatic surface potential (ESP) maps of central units for the central units of GM-series molecules. (d) Monomolecular single crystallographic structure of GM4 in top- and side-view. (e) Single-crystal packing topological structures from top view. (f) The main intermolecular packing modes.

While GM4 exhibits a larger crystal coherence length (CCLs) of 23.56 Å for the (010) in OOP direction, indicative of enhanced crystallinity for GM4, which is helpful to tune the morphology of the active layer. This is consistent with the observed larger electron mobility (μ_e) for GM4 films (3.71×10^{-4} cm^2 V^{-1} s^{-1}) compared to that of 2.89×10^{-4} cm^2 V^{-1} s^{-1} for L8-BO (Figure S3).

Figure 2a and Figure S4 show the normalized absorption spectra of GM2, GM3, GM4, and L8-BO in both neat films and solutions. In dilute chloroform solution, the GM-series acceptor exhibits red-shifted maximum absorption wavelength (λ_{max}) due to an extended molecular skeleton. In the solid state, both the GM-series acceptor and L8-BO display a distinct shoulder peak, indicating effective intermolecular π-π stacking in all the molecules. It is important to note that GM4 shows the smallest redshift ($\Delta\lambda$ = 62 nm) when transitioning from solution to film than the GM2 ($\Delta\lambda$ = 66 nm), GM3 ($\Delta\lambda$ = 71 nm) and L8-BO ($\Delta\lambda$ = 72 nm). This indicates weaker intermolecular π-π stacking in GM4, likely owing to its nonplanar central units and steric hindrance caused by the bromine atom. The HOMO and LUMO energy levels of D18, GM2, GM3, GM4, and L8-BO, derived from cyclic voltammetry under the identical conditions (Figure S5), were calculated to be −5.46/−2.96, −5.68/−3.78, −5.64/−3.79, −5.70/−3.81, and −5.66/−3.87 eV, respectively (Figure 2b and Table S4). Among them, GM4 exhibits the deepest HOMO energy level which will theoretically offer a larger driving force for exciton splitting. Besides, the high LUMO energy level of GM4 enables potentially higher V_{OC}. It is worth noting that GM4 and L8-BO show a cascade energetic structure within the blends, which is beneficial for facilitating charge transport in the ternary blends [33].

2.2 Photovoltaic performance

Given the well-matched energy levels and complementary absorption properties, the polymer donor D18 (with its chemical structure depicted in Figure S6) was used to fabricate OSCs. Detailed device fabrication and optimization processes are outlined in the Supporting Information (Tables S5 and S6). The optimal *J*-*V* characteristics and derived photovoltaic parameters are shown in Figure 2c and Table 1, respectively. The GM4-based binary OSCs attained a satisfactory PCE of 16.5%, featuring a remarkable V_{OC} of 0.975 V, a J_{SC} of 24.6 mA cm^{-2}, and an FF of 68.8%. Its high V_{OC}, reaching near 82% of the S-Q limit, represents one of the best in high-performance systems. Additionally, control devices incorporating GM2 and GM3 demonstrated similarly high V_{OC} of 0.993 and

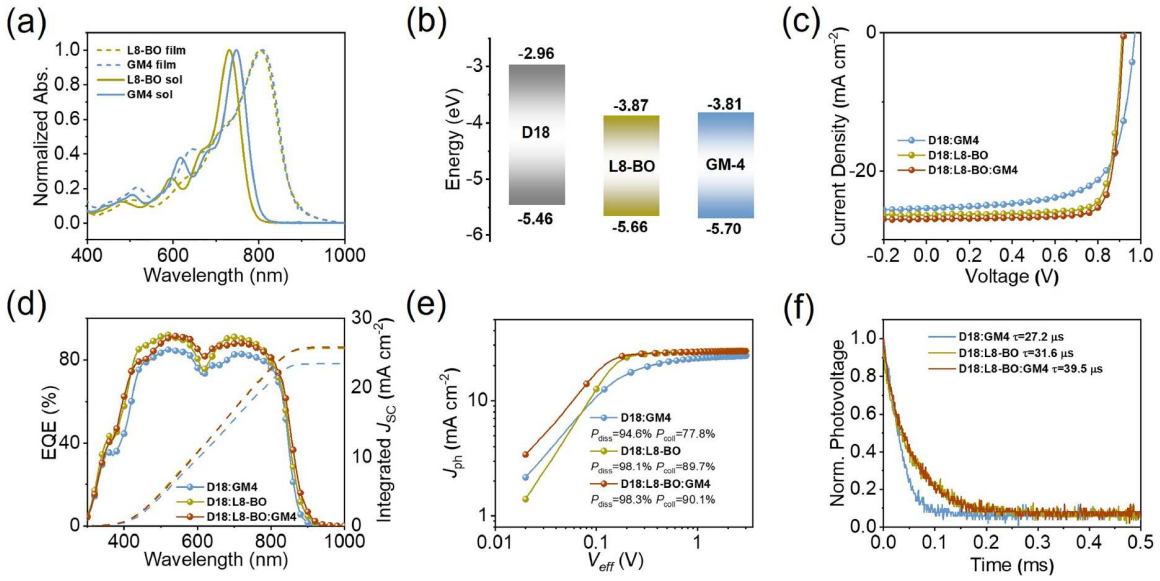

Figure 2 (Color online) (a) UV-vis spectra for GM4 and L8-BO in solutions and solid films. (b) Energy levels of D18, GM4, and L8-BO derived from CV measurements. (c) *J-V* curves for champion OSCs. (d) EQE plots and integrated J_{SC} curves. (e) J_{ph} *versus* V_{eff} curves indicating P_{diss} and P_{coll}. (f) Transient photovoltage (TPV) measurements of the devices.

Table 1 Summary of photovoltaic parameters for OSCs

Active layers	V_{OC} (V)	J_{SC} (mA cm^{-2})	$J_{SC,CAL}$ (mA cm^{-2})	FF (%)	PCE (%)
D18:GM4	0.975	24.6	23.4	68.8	16.5
D18:L8-BO	0.910	26.6	25.7	80.6	19.5
D18:L8-BO:GM4	0.921	26.9	25.9	81.5	20.2

0.982 V (Table S7), indicating the effectiveness of our molecular design strategy for obtaining high V_{OC} acceptors. However, their poor J_{SC} and FF constrained their overall PCEs as well as their potential as the third component in further device optimization. Given the high V_{OC} and reduced energy loss (as discussed below) of D18:GM4 devices, GM4 was incorporated as the third component into the D18:L8-BO binary system. As a result, the ternary system gains a higher V_{OC} of 0.921 V than that of D18:L8-BO binary system (0.910 V). Notably, the introduction of GM4 also broadens the photo-electrical response range of D18:L8-BO host binary blends, which will be further evidenced by the following external quantum efficiency (EQE) discussion. Furthermore, GM4 with high crystallinity effectively regulates the morphology, resulting in increased J_{SC} (26.9 mA cm^{-2}) and FF (81.5%), better than the binary system (J_{SC} of 26.6 mA cm^{-2}, and FF of 80.6%). Overall, this ternary strategy successfully enhanced the V_{OC}, J_{SC}, and FF simultaneously, which increases the PCE of 19.5% for D18:L8-BO binary device to the outstanding PCE of 20.2% of the D18:L8-BO:GM4 ternary devices.

To validate the accuracy of the *J-V* measurements, EQE spectra were also obtained (Figure 2d and Figure S7). The GM-4-based binary system exhibited higher EQE values than those of GM2 and GM3. Notably, the ternary system exhibited a slightly broader, red-shifted EQE response compared to the GM4 and L8-BO-based binary systems, benefiting from the regulation of packing behavior with highly crystalline GM4. The broader EQE curve facilitates the attainment of a higher J_{SC}. Additionally, the EQEs of the ternary devices were considerably higher in the 580–640 nm range, indicating an efficient photoelectric conversion process owing to the incorporation of GM4. Ultimately, the EQE values recorded for the ternary devices reached approximately 90%, which is higher than that of the binary devices. The calculated current densities ($J_{SC,\ CAL}$) derived from EQE curves are 23.4, 25.7, and 25.9 mA cm^{-2} for the D18:GM4, D18:L8-BO, and D18:L8-BO:GM4 devices, respectively. As the incorporation of GM4 to the D18:L8-BO system, the $J_{SC,\ CAL}$ has increased by 0.2 mA cm^{-2}, which agrees with the trend extracted from the *J-V* curves. These results are in good agreement with those derived from the *J-V* curves, supporting the reliability of the findings.

To disclose the underlying reasons behind the differing photovoltaic performances of the binary and ternary devices. The exciton dissociation probability (P_{diss}) and charge collection efficiency (P_{coll}) were evaluated by plotting the photocurrent density (J_{ph}) *versus* the effective voltage (V_{eff}). As shown in Figure 2e, the ternary device exhibited superior performance, showing a P_{diss} of 98.3% and P_{coll} of 90.1%. The improved P_{diss} was attributed to the downshifted HOMO energy levels of GM4, which theoretically provided a large driving force for exciton dissociation. By analyzing the relationship between V_{OC} and J_{SC} with light intensity (Figure S8), the values of n and α for D18:GM4-, D18:L8-BO-, and D18:L8-BO:GM4-based OSCs were determined to be 1.16 and 0.996, 1.18 and 0.998, and 1.17 and 0.996, respectively. These results suggested that the inclusion of GM4 did not induce additional charge-trap-assisted recombination. To further investigate the charge carrier properties in the photovoltaic devices, transient photocurrent (TPC) and transient photovoltage (TPV) measurements were performed, as shown in Figure 2f and Figure S9. As shown in the photocurrent decay curve, the ternary device and L8-BO-based device exhibited a charge extraction time of 0.56 and 0.63 μs, respectively. This indicated that the ternary device showed faster charge extraction and fewer trapped charges. Additionally, the charge carrier lifetime was longer in the ternary devices than in the L8-BO-based devices. Subsequently, the electron/hole mobilities (μ_e/μ_h) of D18:GM4/L8-BO were evaluated by employing the space-charge limited current

(SCLC) method [34], which can be determined to be 4.58/2.19 and 7.29/4.55× 10^{-4} cm^2 V^{-1} s^{-1}, corresponding to μ_e/μ_h ratios of 2.09 and 1.60, respectively (Figure S10). With the incorporation of GM4, the ternary device displays higher carrier mobilities with a μ_e of 7.49 × 10^{-4} cm^2 V^{-1} s^{-1} and a μ_e of 4.66 × 10^{-4} cm^2 V^{-1} s^{-1}, giving a μ_h/μ_e ratio of 1.61. These findings confirmed the enhanced charge carrier generation and charge transport, and suppressed charge carrier recombination in the ternary device, which ultimately contributed to its improved performance.

2.3 Energy loss analysis

As discussed above, the ternary system obtains red-shifted EQE response while an enhanced V_{OC} was achieved in comparison with the host D18:L8-BO binary blend. Herein, an energy loss analysis was performed to investigate the effect of GM4 on the V_{OC}. The relevant data are shown in Figure 3a–c and Table S8. The total E_{loss} was measured to be 0.493 eV for D18:GM4 and 0.548 eV for D18:L8-BO binary OSCs. According to the S-Q theory, the E_{loss} can be divided into three components: ΔE_1, ΔE_2, and ΔE_3 [35]. ΔE_1 represents the unavoidable radiative loss resulting from absorption above the bandgap, ΔE_2 corresponds to the radiative energy loss resulting from absorption below the bandgap, and ΔE_3 represents the nonradiative recombination energy loss. As shown in Figure 3d, the binary systems exhibited the same ΔE_1 of 0.268 eV, but the GM4-based device demonstrated a lower ΔE_2 of 0.050 eV compared to the L8-BO-based device (0.072 eV). Consequently, the GM4-based device showed a ΔE_3 of 0.175 eV, considerably lower than the ΔE_3 of the L8-BO-based device (0.207 eV). These results in ΔE_3 were further confirmed by their EQE_{EL} values (Figure 3e), in which GM4-based devices showed obviously higher EQE_{EL} than L8-BO-based devices. Meanwhile, the D18:GM4-based OSC demonstrated a lower Urbach energy (E_u) of 23.11 meV compared to the D18:L8-BO-based OSC with the E_u of 25.74 meV (Figure S11). This indicated that the regulated aggregated structure of the active layer in the GM4-based system played a crucial role in reducing energy loss. Moreover, the Stokes shift was also calculated to study the influence of molecular structure on energy losses. According to the absorption and PL spectra (Table S9), GM4 exhibits the smaller Stokes shift of 166 nm than that of L8-BO (186 nm), which agrees well with the trend of energy loss. The smaller Stokes shift implies reduced excited-state relaxation, which is beneficial for suppressing voltage losses [36]. Additionally, PLQY measurements of pristine NFAs revealed that GM4 exhibited a higher PLQY of 8.71% compared to L8-BO (4.98%) (Table S10). The higher PLQY of GM4 contributed to lower ΔE_3 values observed in the corresponding devices. It is worth noting that the GM4-based binary system is one of the best for OSCs with low ΔE_3 and high V_{OC}, thus far (Figure 3f and Table S11) [23,27,29,37–58]. When GM4 was incorporated in the D18:L8-BO blend film, the corresponding ternary device showed decreased ΔE_2 and ΔE_3, resulting in a reduced E_{loss} of 0.528 eV and a higher V_{OC} in the corresponding ternary device.

2.4 Charge carrier dynamics

To investigate the exciton diffusion and charge generation processes in the blend films, the transient absorption spectra (TAS) were measured [59,60]. An 800 nm pump beam was used to selectively excite the acceptor, based on the absorption regions of the donor and acceptor. The 2D color plots of the TA images for the L8-BO-based binary and ternary blends are shown in Figure 4a, b. Upon photoexcitation, both films display an excited-state absorption peak around 890 nm with positive signals, along with the rapid appearance of ground-state bleaching (GSB) signals of D18 in the 500–620 nm range. This indicates that hole transfer from the acceptor to the donor occurs in the blend film. To quantitatively assess the hole transfer kinetics, the characteristic time constants τ_1 and τ_2 were obtained by fitting the GSB signals at 600 nm with a double exponential function (Figure 4c). The results are as follows: D18:L8-BO (τ_1 = 1.15 ± 0.19 ps, τ_2 = 13.97 ± 2.36 ps) and D18:L8-BO:GM4 (τ_1 = 1.05 ± 0.17 ps, τ_2 = 11.97 ± 1.42 ps). The τ_1 corresponds to the rapid process related to excitons generated in the mixed phase, while τ_2 represents the slower process for photo-induced excitons diffusing to the D/A interface. It was observed that both systems exhibit similar rapid processes. The ternary blend film exhibits a slightly shorter τ_2. This improved exciton diffusion rate in the ternary film may be attributed to the optimal domain size, which leads to refined phase separation and is favorable for exciton dissociation.

Additionally, the ternary system shows a longer carrier lifetime

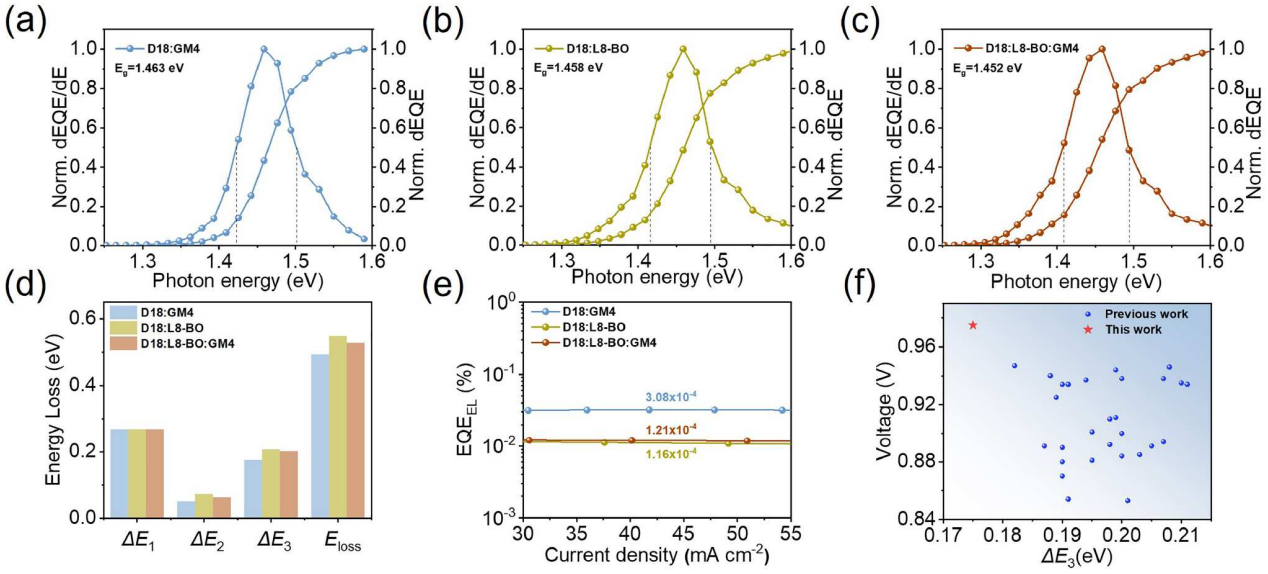

Figure 3 (Color online) Optical bandgap determination of (a) D18:GM4, (b) D18:L8-BO, and (c) D18:L8-BO:GM4 blend films on the basis of the derivatives of the sensitive EQE spectra (dEQE/dE) for optimized OSCs. (d) Statistical diagram of detailed E_{loss} of D18:GM4, D18:L8-BO, and D18:L8-BO:GM4-based devices. (e) The corresponding EQE_{EL} spectra for optimized OSCs. (f) Summary of V_{OC} and ΔE_3 for binary OSCs from the literature and this work [23,27,29,37–58].

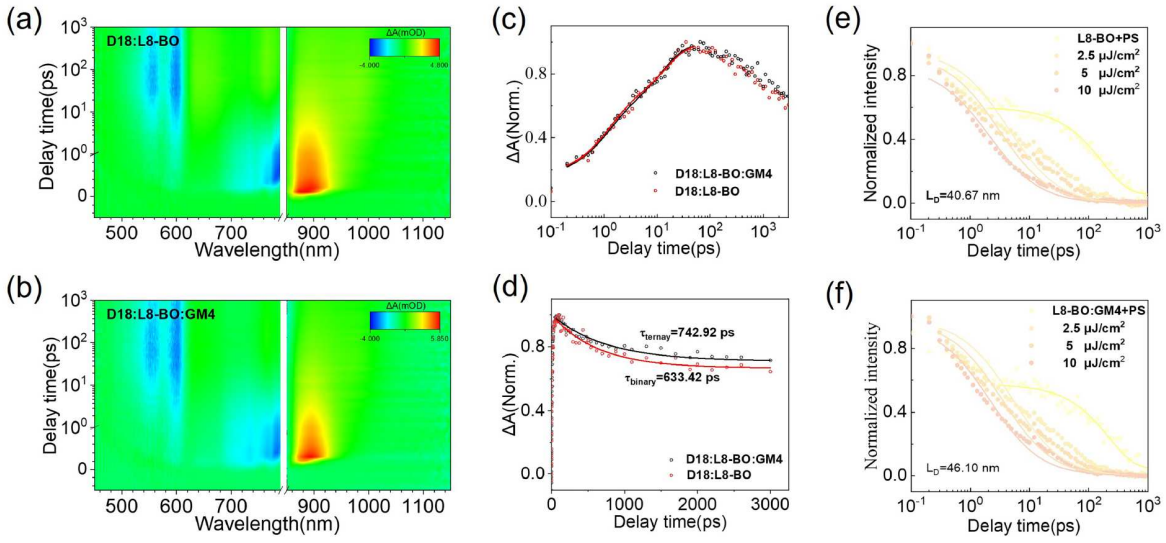

Figure 4 (Color online) (a, b) Contour plots of the time-resolved absorption difference spectra of the blend films. (c) Rising kinetics observed at 600 nm, indicative of the hole transfer process. (d) The carrier lifetime of the blend film. (e) The corresponding EQE_{EL} spectra for optimized OSCs. (f) Dynamics of the singlet excitons.

(742.92 ps) compared to the binary system (633.42 ps) (Figure 4d). Furthermore, a photoluminescence (PL) quenching measurement was performed to assess charge-transfer efficiency. As shown in Figure S12, three types of acceptor film display relatively high PL intensity. After blending with donor D18, GM4, and L8-BO, and ternary-based blend films exhibit quenching efficiencies of 88.0%, 90.7%, and 90.6%, respectively. The results show that the introduction of GM4 maintains a high charge-transfer efficiency. Exciton diffusion lengths (L_D) were also estimated using the exciton-exciton annihilation (EEA) method through pump-fluence-dependent TAS. The L_D was calculated using the equation: $L_D = \sqrt{D\tau}$, where D represents the exciton diffusion coefficient. As shown in Figure 4e, f, the ternary system exhibits a longer L_D (46.1 nm) compared to the L8-BO-based binary system (40.7 nm), indicating a higher probability for excitons to diffuse to the D/A interfaces. All these results demonstrate that the D18:L8-BO:GM4-based system provides the highest exciton dissociation and transport, which contributes to superior J_{SC} and FF.

2.5 Morphology analysis

It is well known that morphology plays a critical role in regulating charge transport behavior and achieving outstanding photovoltaic performance. Therefore, atomic force microscopy-based infrared spectroscopy (AFM-IR) was used to monitor the film morphology. As shown in Figure S13, all the blend films exhibit a uniform and smooth surface. The root-mean-square roughness values for D18:GM4, D18:L8-BO, and D18:L8-BO:GM4 are 1.43, 0.89, and 1.00 nm, respectively. The AFM-IR phase images revealed the distributions of the donor and acceptor materials, as well as the morphology, by analyzing the infrared absorption peak at 2216 cm^{-1}, which is unique to the stretching vibration of the C≡N bond in the acceptors. Figure 5a–c shows clear nanoscale fiber structures in all blend films, facilitating the exciton dissociation and charge transport processes. Through statistical analysis, the average fibril diameters for D18:GM4, D18:L8-BO, and D18:L8-BO:GM4 were determined to be 13.15, 11.38, and 12.44 nm (Figure 5d–f and Figure S14), respectively, suggesting that GM4 has improved crystallinity and effectively tuned phase separation of ternary blend films. The moderate fibril diameters in the ternary blend films promote high charge mobility and efficient charge transport.

Given that the D/A phase separation size is closely related to the miscibility between donor and SMAs, the contact angles were measured, and the corresponding Flory-Huggins interaction parameters (χ) were further derived, with the results displayed in Figure S15 and Table S12. The $\chi_{D\text{-}A}$ value for D18:GM4 is 0.08, which is larger than that for D18:L8-BO (0.04), indicating lower D/A miscibility for the GM4 and D18. This may contribute to the higher domain purity and larger nanofiber size, which aligns well with the results from the AFM-IR images.

2.6 Molecular dynamics

To investigate the interaction between the donor and acceptor, molecular dynamics simulations were used (Figure 5g–i). As shown in Figure S16, D18 was divided into two segments, labeled C and E, while GM4 and L8-BO were divided into four segments, labeled A, D, and A′. This resulted in six distinct packing modes. Radial distribution functions (RDFs) between D18 and these acceptors were calculated to study the molecular packing behavior. As shown in Figure S17, both GM4- and L8-BO-based binary systems displayed favorable RDF peaks. In the ternary system, the RDF shows a pronounced peak corresponding to the interaction between D18 and GM4, indicating that the formation of an ordered structure is facilitated by the introduction of GM4. Furthermore, the stacking counts per unit volume for these three systems were calculated (Tables S13 and S14). Both binary systems show comparable counts for face-on stacking and total stacking. Notably, the considerable differences in stacking distribution can be attributed to the stacking interactions between D18 and the A′ segment of GM4. When considering total stacking, the counts for the CA′ and EA′ segments of GM4 are higher than those of L8-BO. The result may be attributed to the interaction between the bromine atom of the central unit and the heteroatom of the donor backbone. In the ternary system, the total and face-on stacking counts show intermediate values between those of the two binary systems, indicating that the addition of GM4 adjusts the stacking density and promotes structural order. This, in turn, enhances the PCE of the devices.

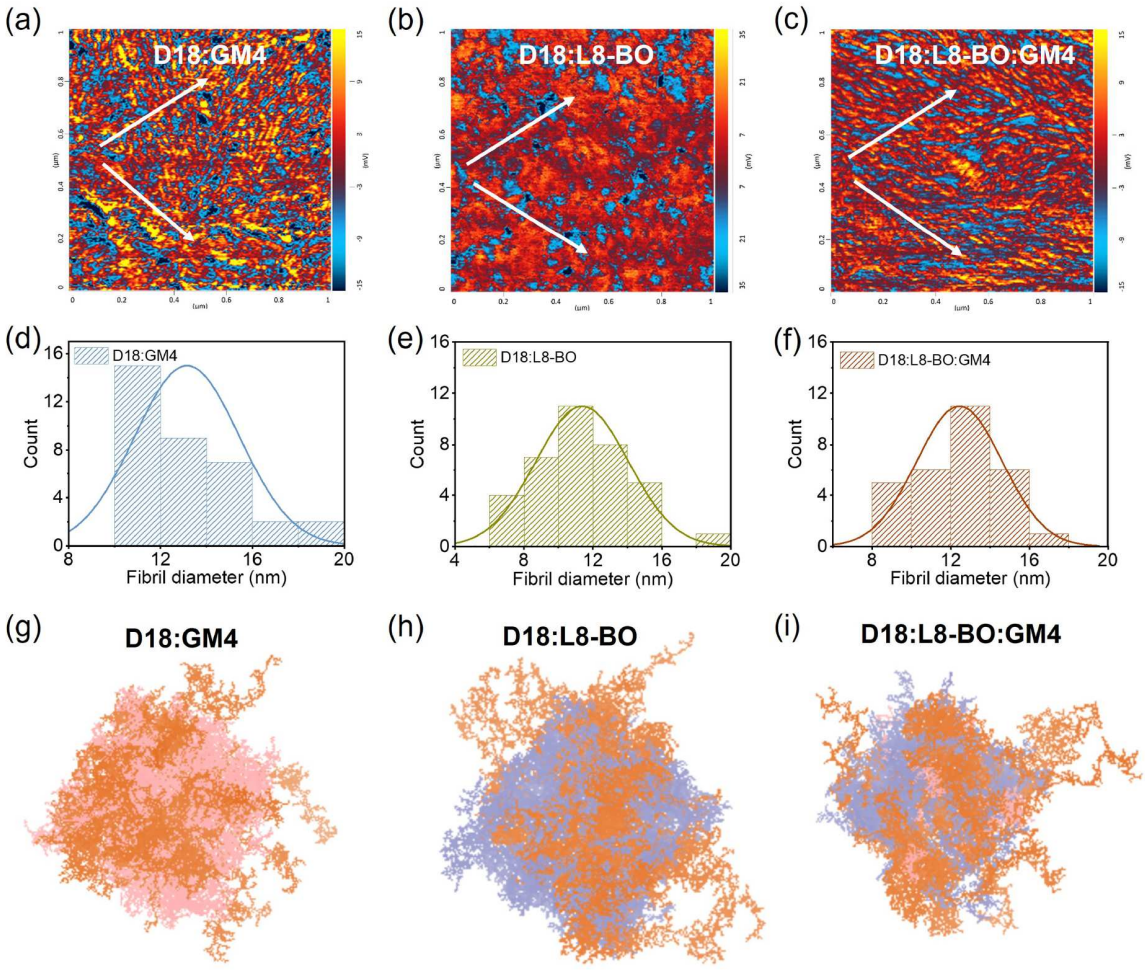

Figure 5 (Color online) (a–c) AFM-IR phase images of three blended films by detecting 2216 cm^{-1} signal of acceptors, in which donor and acceptor domains were marked with blue and red colors, respectively. (d–f) Statistical distribution of phase separation sizes. (g–i) MD simulation of the structure of three systems, where the pink, blue and orange colors correspond to GM4, L8-BO and D18, respectively.

3 Conclusions

In this study, we developed a novel approach to reconstruct fused-ring aromatic backbones of Y-series SMA, leading to the successful synthesis of novel A-D-A-type acceptors. The new electronic structure of GM4 exhibits unique photoelectric properties that effectively minimize the ΔE_3 and maximize device performance. Note that the subtle synthesis strategy of GM4 establishes a versatile molecular platform for further structural modifications. Single-crystal analysis demonstrates that GM4 exhibits a distorted conformation with reduced packing density, which contributes to its exceptional PLQY and low ΔE_3 of 0.175 eV. Additionally, the strategic bromination of the central unit effectively enhanced molecular crystallinity, which facilitates optimized morphology. Besides, the nonplanar central unit contributed to a packing mode in the single crystal, which is partly responsible for establishing the optimal 3D intermolecular packing network, enabling effective charge dynamics and highly efficient performance. When blended with the polymer donor D18, the resulting D18:GM4 OSC achieved a PCE of 16.5% with a high V_{OC} of 0.975 V, reaching nearly 82% of the S-Q limit. Due to its high crystallinity, GM4 incorporated in the D18:L8-BO blend successfully tuned the morphology, leading to improved exciton dissociation, diffusion, and charge transfer. As a result, the corresponding OSC achieved an excellent PCE of 20.2%, V_{OC} of 0.921 V, J_{SC} of 26.9 mA cm^{-2}, and FF of 81.5%. This work demonstrates an effective strategy of balancing molecular planarity, packing density, and crystallinity for designing high-performance acceptors with a high PLQY and crystallinity, paving the way for realizing high-performance OSCs with high V_{OC} and reduced E_3.

Conflict of interest

The authors declare no conflict of interest.

Acknowledgement

This work was supported by the Ministry of Science and Technology of China (2023YFE0210400), the National Natural Science Foundation of China (22361132530, 52025033, 52303237, 52373189), the Natural Science Foundation of Tianjin (24JCYBJC01540) and the Fundamental Research Funds for the Central Universities of Nankai University (023-63253172).

Supporting information

The supporting information is available online at http://chem.scichina.com and http://link.springer.com/journal/11426. The supporting materials are published as submitted, without typesetting or editing. The responsibility for scientific accuracy and content remains entirely with the authors.

References

1 Yang N, Cui Y, Zhang T, An C, Chen Z, Xiao Y, Yu Y, Wang Y, Hao XT, Hou J. *J Am Chem Soc*, 2024, 146: 9205–9215
2 Polman A, Knight M, Garnett EC, Ehrler B, Sinke WC. *Science*, 2016, 352: aad4424
3 Lu X, Xie C, Liu Y, Zheng H, Feng K, Xiong Z, Wei W, Zhou Y. *Nat Energy*, 2024, 9: 793–802
4 Huang T, Geng S, Wang D, Zhang Y, Weng N, Li X, Liao Q, Zhang Z, Lu J, Zhang J. *Adv Funct Mater*, 2024, 34: 2315825
5 Zhu Y, Zhang Z, Si W, Sun Q, Cai G, Li Y, Jia Y, Lu X, Xu W, Zhang S, Lin Y. *J Am Chem Soc*, 2022, 144: 12747–12755
6 Yin H, Cui Y, Chen D, Liu S, Wu T, Yu M, Ye L, Liang A, Chen Y. *J Am Chem Soc*, 2025, 147: 8796–8808
7 Gong Y, Tan S, Li X, Qin S, Li X, Zou T, Li Y, Yuan M, Zhang Z, Hu H, Liang T, Zhang

J, Meng L, Liu F, Li Y. *Angew Chem Int Ed*, 2025, 64: e202505366
8 Yuan J, Zhang Y, Zhou L, Zhang G, Yip HL, Lau TK, Lu X, Zhu C, Peng H, Johnson PA, Leclerc M, Cao Y, Ulanski J, Li Y, Zou Y. *Joule*, 2019, 3: 1140–1151
9 Gong Y, Zou T, Li X, Zhuo H, Qin S, Sun G, Meng L, Li Y. *Sci China Chem*, 2023, 66: 2912–2920
10 Tian H, Sun K, Luo D, Wang Y, Chen Z, Yu L, Zhang G, Yang C, Luo Z. *Sci China Chem*, 2025, 68: 6628–6638
11 Chen H, Huang Y, Zhang R, Mou H, Ding J, Zhou J, Wang Z, Li H, Chen W, Zhu J, Cheng Q, Gu H, Wu X, Zhang T, Wang Y, Zhu H, Xie Z, Gao F, Li Y, Li Y. *Nat Mater*, 2025, 24: 444–453
12 Cheng B, Xia X, Cheng S, Han C, Sun F, Fu Z, Hou W, Hua F, Wang H, Sun W, Huo Y, Ji S, Guo X, Yin H, Du X, Hao X, Li Y, Zhang M. *Adv Mater*, 2025, 37: 2500357
13 Zhu L, Zhang M, Xu J, Li C, Yan J, Zhou G, Zhong W, Hao T, Song J, Xue X, Zhou Z, Zeng R, Zhu H, Chen CC, MacKenzie RCI, Zou Y, Nelson J, Zhang Y, Sun Y, Liu F. *Nat Mater*, 2022, 21: 656–663
14 Lin Y, Firdaus Y, Isikgor FH, Nugraha MI, Yengel E, Harrison GT, Hallani R, El-Labban A, Faber H, Ma C, Zheng X, Subbiah A, Howells CT, Bakr OM, McCulloch I, Wolf SD, Tsetseris L, Anthopoulos TD. *ACS Energy Lett*, 2020, 5: 2935–2944
15 Wang X, Liang Q, Zhang A, Wei N, Jiang H, Cheng Y, Fang H, Li S, Lu H, Li W, Bo Z. *J Am Chem Soc*, 2025, 147: 9261–9272
16 Shafe AA, Raza S, Henry R, Liu J, O'Connor BT. *ACS Energy Lett*, 2025, 10: 1865–1873
17 Zheng Z, Wang J, Bi P, Ren J, Wang Y, Yang Y, Liu X, Zhang S, Hou J. *Joule*, 2022, 6: 171–184
18 He Z, Zhong C, Su S, Xu M, Wu H, Cao Y. *Nat Photon*, 2012, 6: 591–595
19 Zhou M, Liao C, Duan Y, Xu X, Yu L, Li R, Peng Q. *Adv Mater*, 2023, 35: 2208279
20 Zhan L, Li S, Li Y, Sun R, Min J, Bi Z, Ma W, Chen Z, Zhou G, Zhu H, Shi M, Zuo L, Chen H. *Joule*, 2022, 6: 662–675
21 Chen XK, Qian D, Wang Y, Kirchartz T, Tress W, Yao H, Yuan J, Hülsbeck M, Zhang M, Zou Y, Sun Y, Li Y, Hou J, Inganäs O, Coropceanu V, Bredas JL, Gao F. *Nat Energy*, 2021, 6: 799–806
22 Gillett AJ, Privitera A, Dilmurat R, Karki A, Qian D, Pershin A, Londi G, Myers WK, Lee J, Yuan J, Ko SJ, Riede MK, Gao F, Bazan GC, Rao A, Nguyen TQ, Beljonne D, Friend RH. *Nature*, 2021, 597: 666–671
23 Jiang Y, Li Y, Liu F, Wang W, Su W, Liu W, Liu S, Zhang W, Hou J, Xu S, Yi Y, Zhu X. *Nat Commun*, 2023, 14: 5079
24 Li S, Zhan L, Yao N, Xia X, Chen Z, Yang W, He C, Zuo L, Shi M, Zhu H, Lu X, Zhang F, Chen H. *Nat Commun*, 2021, 12: 4627
25 Chen G, Li W, Zhou T, Peng Q, Zhai D, Li H, Yuan WZ, Zhang Y, Tang BZ. *Adv Mater*, 2015, 27: 4496–4501
26 Lu H, Li D, Liu W, Ran G, Wu H, Wei N, Tang Z, Liu Y, Zhang W, Bo Z. *Angew Chem Int Ed*, 2024, 63: e202407007
27 Chen H, Zou Y, Liang H, He T, Xu X, Zhang Y, Ma Z, Wang J, Zhang M, Li Q, Li C, Long G, Wan X, Yao Z, Chen Y. *Sci China Chem*, 2022, 65: 1362–1373
28 Zhang Z, Feng W, Zhang Y, Yuan S, Bai Y, Wang P, Yao Z, Li C, Duan T, Wan X, Kan B, Chen Y. *Sci China Chem*, 2024, 67: 1596–1604
29 Shi Y, Chang Y, Lu K, Chen Z, Zhang J, Yan Y, Qiu D, Liu Y, Adil MA, Ma W, Hao X, Zhu L, Wei Z. *Nat Commun*, 2022, 13: 3256
30 Zhu W, Spencer AP, Mukherjee S, Alzola JM, Sangwan VK, Amsterdam SH, Swick SM, Jones LO, Heiber MC, Herzing AA, Li G, Stern CL, DeLongchamp DM, Kohlstedt KL, Hersam MC, Schatz GC, Wasielewski MR, Chen LX, Facchetti A, Marks TJ. *J Am Chem Soc*, 2020, 142: 14532–14547
31 Li C, Song J, Lai H, Zhang H, Zhou R, Xu J, Huang H, Liu L, Gao J, Li Y, Jee MH, Zheng Z, Liu S, Yan J, Chen XK, Tang Z, Zhang C, Woo HY, He F, Gao F, Yan H, Sun Y. *Nat Mater*, 2025, 24: 433–443
32 Li C, Zhou J, Song J, Xu J, Zhang H, Zhang X, Guo J, Zhu L, Wei D, Han G, Min J, Zhang Y, Xie Z, Yi Y, Yan H, Gao F, Liu F, Sun Y. *Nat Energy*, 2021, 6: 605–613
33 Chen C, Wang L, Sun Y, Fu Y, Guo C, Zhou B, Gan Z, Liu D, Li W, Wang T. *Adv Funct Mater*, 2023, 33: 2305765
34 Zhao X, An Q, Zhang H, Yang C, Mahmood A, Jiang M, Jee MH, Fu B, Tian S, Woo HY, Wang Y, Wang J. *Angew Chem Int Ed*, 2023, 62: e202216340
35 Yao J, Kirchartz T, Vezie MS, Faist MA, Gong W, He Z, Wu H, Troughton J, Watson T, Bryant D, Nelson J. *Phys Rev Appl*, 2015, 4: 014020
36 Gu X, Wei Y, Zeng R, Lv J, Hou Y, Yu N, Tan S, Wang Z, Li C, Tang Z, Peng Q, Liu F, Cai Y, Zhang X, Huang H. *Angew Chem Int Ed*, 2025, 64: e202418926
37 Zhang L, Zhang Z, Deng D, Zhou H, Zhang J, Wei Z. *Adv Sci*, 2022, 9: 2202513
38 Shi Y, Pan J, Yu J, Zhang J, Gao F, Lu K, Wei Z. *Sol RRL*, 2021, 5: 2100008
39 Zhang J, Bai F, Angunawela I, Xu X, Luo S, Li C, Chai G, Yu H, Chen Y, Hu H, Ma Z, Ade H, Yan H. *Adv Energy Mater*, 2021, 11: 2102596
40 Wang H, Lu H, Chen Y, Ran G, Zhang A, Li D, Yu N, Zhang Z, Liu Y, Xu X, Zhang W, Bao Q, Tang Z, Bo Z. *Adv Mater*, 2022, 34: 2105483
41 Liu S, Yuan J, Deng W, Luo M, Xie Y, Liang Q, Zou Y, He Z, Wu H, Cao Y. *Nat Photon*, 2020, 14: 300–305
42 Liu K, Jiang Y, Ran G, Liu F, Zhang W, Zhu X. *Joule*, 2024, 8: 835–851
43 Lu H, Liu W, Ran G, Liang Z, Li H, Wei N, Wu H, Ma Z, Liu Y, Zhang W, Xu X, Bo Z. *Angew Chem Int Ed*, 2023, 62: e202314420
44 He C, Shen Q, Wu B, Gao Y, Li S, Min J, Ma W, Zuo L, Chen H. *Adv Energy Mater*, 2023, 13: 2204154
45 Qiu D, Zhang H, Tian C, Zhang J, Zhu L, Wei Z, Lu K. *Adv Mater*, 2023, 35: 2307398
46 Si X, Huang Y, Shi W, Wang R, Ma K, Zhang Y, Wu S, Yao Z, Li C, Wan X, Chen Y. *Adv Funct Mater*, 2023, 33: 2306471
47 Fan B, Gao W, Zhang R, Kaminsky W, Lin FR, Xia X, Fan Q, Li Y, An Y, Wu Y, Liu M, Lu X, Li WJ, Yip HL, Gao F, Jen AKY. *J Am Chem Soc*, 2023, 145: 5909–5919
48 Bi X, Li S, He T, Chen H, Li Y, Jia X, Cao X, Guo Y, Yang Y, Ma W, Yao Z, Kan B, Li C, Wan X, Chen Y. *Small*, 2024, 20: 2311561
49 Jiang Y, Sun S, Xu R, Liu F, Miao X, Ran G, Liu K, Yi Y, Zhang W, Zhu X. *Nat Energy*, 2024, 9: 975–986
50 Bai Y, Chen T, Ji X, Wang J, Zhao W, Yuan S, Zhang Y, Long G, Zhang Z, Wan X, Kan B, Chen Y. *Adv Energy Mater*, 2024, 14: 2400938
51 Liu J, Duan X, Song J, Liu C, Gao J, Jee MH, Tang Z, Woo HY, Sun Y. *Energy Environ Sci*, 2024, 17: 3641–3650
52 Bi P, Zhang T, Cui Y, Wang J, Qiao J, Xian K, Chua XW, Chen Z, Goh WP, Ye L, Hao X, Hou J, Yang L. *Adv Energy Mater*, 2023, 13: 2302252
53 Zhang Z, Yuan S, Chen T, Wang J, Yi YQQ, Zhao B, Li M, Yao Z, Li C, Wan X, Long G, Kan B, Chen Y. *Energy Environ Sci*, 2024, 17: 5719–5729
54 Duan T, Feng W, Li Y, Li Z, Zhang Z, Liang H, Chen H, Zhong C, Jeong S, Yang C, Chen S, Lu S, Rakitin OA, Li C, Wan X, Kan B, Chen Y. *Angew Chem Int Ed*, 2023, 62: e202308832
55 Chen Z, Zhang S, Zhang T, Ren J, Dai J, Li H, Qiao J, Hao X, Hou J. *Angew Chem Int Ed*, 2024, 63: e202317892
56 Liu F, Jiang Y, Xu R, Su W, Wang S, Zhang Y, Liu K, Xu S, Zhang W, Yi Y, Ma W, Zhu X. *Angew Chem Int Ed*, 2024, 63: e202313791
57 Liu W, Xu X, He S, Sun R, Chen Q, Min J, Zhang Z, Yuan J, Li Y, Zou Y. *Macromolecules*, 2023, 56: 8623–8631
58 Liu K, Jiang Y, Liu F, Ran G, Huang F, Wang W, Zhang W, Zhang C, Hou J, Zhu X. *Adv Mater*, 2023, 35: 2300363
59 Guo Z, Lee D, Schaller RD, Zuo X, Lee B, Luo TF, Gao H, Huang L. *J Am Chem Soc*, 2014, 136: 10024–10032
60 Chen Z, Chen X, Qiu B, Zhou G, Jia Z, Tao W, Li Y, Yang YM, Zhu H. *J Phys Chem Lett*, 2020, 11: 3226–3233